

TEMPERATURE PROFILES AND THE EFFECT OF AGN ON SUBMILLIMETER EMISSION FROM BLAST OBSERVATIONS OF RESOLVED GALAXIES

DONALD V. WIEBE,^{1,2} PETER A. R. ADE,³ JAMES J. BOCK,^{4,5} EDWARD L. CHAPIN,¹ MARK J. DEVLIN,⁶ SIMON DICKER,⁶ MATTHEW GRIFFIN,³ JOSHUA O. GUNDERSEN,⁷ MARK HALPERN,¹ PETER C. HARGRAVE,³ DAVID H. HUGHES,⁸ JEFF KLEIN,⁶ GAELLEN MARSDEN,¹ PETER G. MARTIN,^{9,10} PHILIP MAUSKOPF,³ CALVIN B. NETTERFIELD,^{2,10} LUCA OLMI,^{11,12} ENZO PASCALE,³ GUILLAUME PATANCHON,¹³ MARIE REX,⁶ DOUGLAS SCOTT,¹ CHRISTOPHER SEMISCH,⁶ NICHOLAS THOMAS,⁷ MATTHEW D. P. TRUCH,⁶ CAROLE TUCKER,³ GREGORY S. TUCKER,¹⁴ MARCO P. VIERO¹⁰

To appear in The Astrophysical Journal

ABSTRACT

Over the course of two flights, the Balloon-borne Large Aperture Submillimeter Telescope (BLAST) made resolved maps of seven nearby (< 25 Mpc) galaxies at 250, 350, and 500 μm . During its June 2005 flight from Sweden (BLAST05), BLAST observed a single nearby galaxy, NGC 4565. During the December 2006 flight from Antarctica (BLAST06), BLAST observed the nearby galaxies NGC 1097, NGC 1291, NGC 1365, NGC 1512, NGC 1566, and NGC 1808. We fit physical dust models to a combination of BLAST observations and other available data for the galaxies with *Spitzer* data. We fit a modified blackbody to the remaining galaxies to obtain total dust mass and mean dust temperature. For the four galaxies with *Spitzer* data, we also produce maps and radial profiles of dust column density and temperature. We measure the fraction of BLAST detected flux originating from the central cores of these galaxies and use this to calculate a “core fraction,” an upper limit on the “AGN fraction” of submillimeter detected galaxies. Finally, we are able to use these data to derive a value for the dust mass absorption co-efficient of $\kappa = 0.29 \pm 0.03 \text{ m}^2 \text{ kg}^{-1}$ at 250 μm .

Subject headings: balloons — galaxies: photometry — submillimeter — telescopes

1. INTRODUCTION

Much of the bolometric luminosity produced by entire galaxies is emitted as thermal radiation from dust grains in the interstellar medium (ISM) at temperatures of several tens of Kelvin. The heat source is predominantly optical and ultra-violet (UV) light from stars, as well as matter accretion onto an active galactic nucleus (AGN) in some objects. In either case, the spectrum of this light tends to peak in the range $\sim 60\text{--}200 \mu\text{m}$. Since the launch of the *Infrared Astronomical Satellite* (*IRAS*) in 1983, observations at these wavelengths have been es-

sential in a number of fields, ranging from the studies of the earliest stages of star-formation in dusty molecular clouds in our own Galaxy, to the detection of distant star-forming galaxies that emit most of their light in this previously unexploited band. Furthermore, excluding light from the Cosmic Microwave Background, it is known that approximately half of all of the light in the Universe is emitted at these wavelengths, the Cosmic Infrared Background (CIB) (Puget et al. 1996; Fixsen et al. 1998, see also Devlin et al. 2009).

Observations from the ground are impossible at wavelengths in the range $\sim 60\text{--}200 \mu\text{m}$, the far infrared (far-IR) band, due primarily to the absorption and emission from atmospheric water vapor. Therefore, most of the progress at these wavelengths since *IRAS* has also been undertaken by satellites: the *Infrared Space Observatory* (*ISO*), the *Spitzer Space Telescope*, and the *Akari Space Telescope*. However, the lack of data at longer wavelengths can bias the interpretation of these results toward the assumption of warmer dust temperatures, resulting in underestimates of luminosity and mass. At slightly longer wavelengths, $\sim 350\text{--}1000 \mu\text{m}$, the submillimeter band, several narrow spectral windows are available from dry, high-altitude sites such as Mauna Kea or the Atacama Desert. In particular, studies at 850 μm with SCUBA (Holland et al. 1999) have been used to detect very cool dust, both in our Galaxy, and in more distant galaxies. Typically in these surveys a dust temperature must be assumed in order to estimate temperatures and luminosities, because data is available only at a single wavelength. Therefore the combination of ground-based submillimeter observations with space-based far-IR measurements has been required to assess the bolometric luminosities and apparent dust temperatures of everything from individual pre-stellar objects, up to en-

¹ Department of Physics & Astronomy, University of British Columbia, 6224 Agricultural Road, Vancouver, BC V6T 1Z1, Canada

² Department of Physics, University of Toronto, 60 St. George Street, Toronto, ON M5S 1A7, Canada

³ School of Physics and Astronomy, Cardiff University, 5 The Parade, Cardiff, CF24 3AA, UK

⁴ Jet Propulsion Laboratory, Pasadena, CA 91109-8099

⁵ Observational Cosmology, MS 59-33, California Institute of Technology, Pasadena, CA 91125

⁶ Department of Physics and Astronomy, University of Pennsylvania, 209 South 33rd Street, Philadelphia, PA 19104

⁷ Department of Physics, University of Miami, 1320 Campo Sano Drive, Coral Gables, FL 33146

⁸ Instituto Nacional de Astrofísica Óptica y Electrónica, Aptdo. Postal 51 y 216, 72000 Puebla, Mexico

⁹ Canadian Institute for Theoretical Astrophysics, University of Toronto, 60 St. George Street, Toronto, ON M5S 3H8, Canada

¹⁰ Department of Astronomy & Astrophysics, University of Toronto, 50 St. George Street, Toronto, ON M5S 3H4, Canada

¹¹ Istituto di Radioastronomia, Largo E. Fermi 5, I-50125, Firenze, Italy

¹² University of Puerto Rico, Rio Piedras Campus, Physics Dept., Box 23343, UPR station, San Juan, Puerto Rico

¹³ Laboratoire APC, 10, rue Alice Domon et Léonie Duquet 75205 Paris, France

¹⁴ Department of Physics, Brown University, 182 Hope Street, Providence, RI 02912;

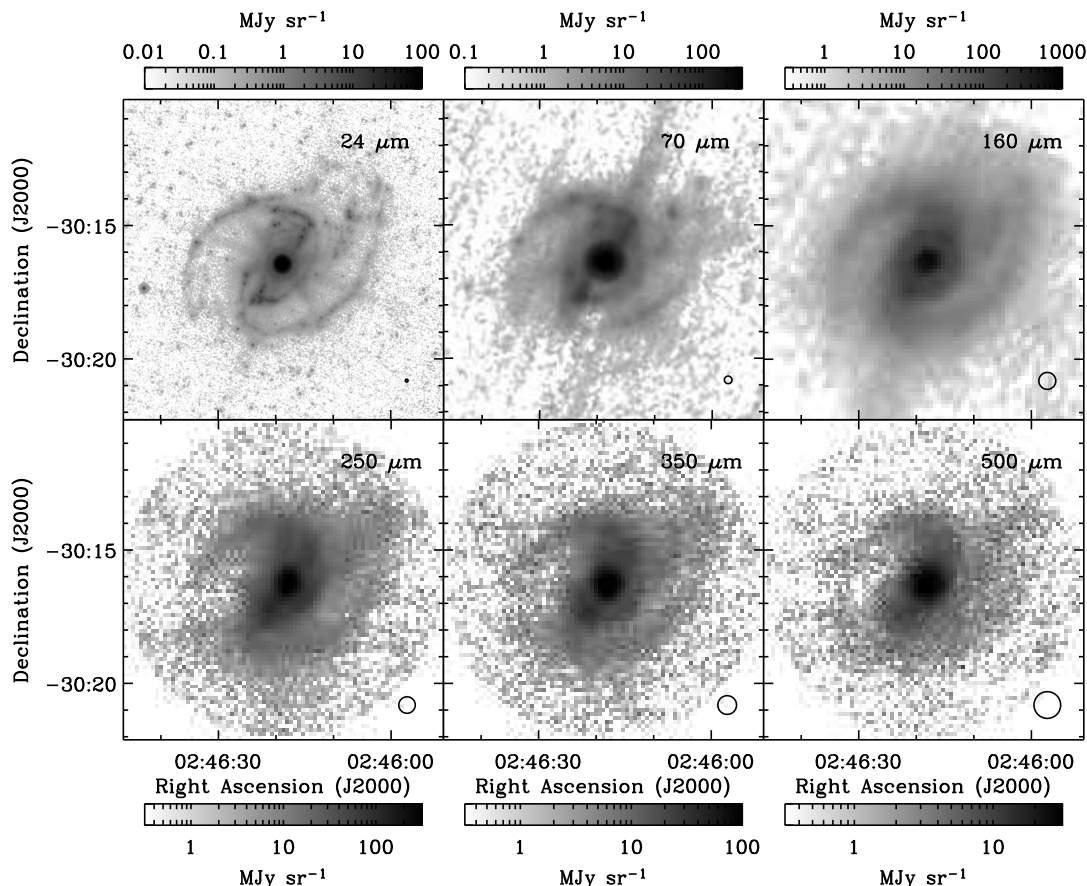


FIG. 1.— BLAST (bottom row) and MIPS (top row) observations of NGC 1097. The radius of the clipped BLAST map is $6'$. The intensity scale is logarithmic. The FWHM size of the BLAST and MIPS beams are plotted for reference in the lower right corner. BLAST resolves the spiral arms and central bar of the galaxy. The $24\text{ }\mu\text{m}$ image is shown for comparison only, and not used in this analysis.

tire galaxies at redshifts $z > 1$. The lack of data in the crucial wavelength range $\sim 200\text{--}500\text{ }\mu\text{m}$ results in large uncertainties in these quantities.

In this paper we present results from a study at 250, 350, and $500\text{ }\mu\text{m}$ of several nearby galaxies using the 2-m Balloon-borne Large Aperture Submillimeter Telescope (BLAST). BLAST was built to fill the wavelength gap between ground-based submillimeter and space-based far-IR instrumentation, using a prototype of the SPIRE camera for *Herschel* (Griffin et al. 2007).

During its first scientific flight, hereafter BLAST05, BLAST, launched from Esrange, Sweden, acquired data for 100 hours before landing on Victoria Island, Canada. During this flight, BLAST observed the nearby galaxy NGC 4565. In December 2006, BLAST conducted its second science flight, BLAST06, carrying out 250 hours of observations above Antarctica. Six nearby galaxies were observed during BLAST06: NGC 1097, NGC 1291, NGC 1365, NGC 1512, NGC 1566, and NGC 1808.

All these galaxies are resolved by BLAST, which had full widths at half-maximum (FWHM) of $36''$, $42''$, and $60''$ at 250, 350, and $500\text{ }\mu\text{m}$ respectively during BLAST06. The single galaxy in our sample from BLAST05 is also resolved despite the large, non-Gaussian point spread functions of the telescope during this flight. We are therefore able to map the temperature and luminosity, and hence dust column density, with greater signal-to-noise ratio (SNR) than any existing study. The study can be considered a precursor to The Herschel Reference Sur-

vey (Boselli et al. 2008) and the JCMT Nearby Galaxies Legacy Survey (Wilson et al. 2009) that will be undertaken by *Herschel* and SCUBA-2, respectively. A complete description of the BLAST instrument is given in Pascale et al. (2008).

The known correlation between temperature and luminosity in *IRAS* galaxies (e.g. Soifer & Neugebauer 1991) means good measurements of these quantities for rest-frame galaxies are required to put proper constraints on high-redshift FIR source count models (e.g. Chapin et al., in prep.). BLAST samples the Rayleigh-Jeans side of thermal emission from local galaxies; when combined with far-IR measurements from other instruments, the dust thermal emission peak is bracketed, allowing robust determination of these quantities.

Resolved studies of galaxies are required to better model galactic structure and dynamics. The unprecedented ability of BLAST to make high resolution maps on large angular scales in the submillimeter band provides the best opportunity to-date to study the structure of diffuse dust in nearby galaxies. To properly estimate star formation rates from submillimeter fluxes of unresolved, high redshift galaxies, an understanding of the fraction of submillimeter flux originating from AGN-driven dust heating is required. BLAST is able to put limits on this AGN fraction by comparing flux measured from the core of these resolved galaxies compared to their total integrated flux. Furthermore, because BLAST can make high-fidelity large-area maps, it is able to mea-

sure the complete emission from these spatially extended galaxies.

2. DATA REDUCTION

The common data reduction pipeline for BLAST has been presented in Truch et al. (2008) and Patanchon et al. (2008). Maps used in this analysis for NGC 4565 were made using the maximum-likelihood map maker SANEPIC (Patanchon et al. 2008) which was written explicitly for BLAST analysis.

Maps of BLAST observations of the remaining galaxies were produced using *Almagest* (Wiebe 2008), an iterative, maximum-likelihood map maker also written for BLAST analysis, and algorithmically similar to other iterative map makers used in CMB analysis (e.g. Prunet et al. 2000). In lieu of cross-linking, the maps produced are artificially constrained to zero flux far from the observed galaxy to improve convergence properties of the iterative algorithm (see §3.8 of Patanchon et al. 2008). In relatively high SNR cases, such as these galaxy maps, *Almagest* maps are consistent with maps made with SANEPIC (Wiebe 2008), but may be produced faster, and allow arbitrary constraints to be applied simply.

3. OBSERVATIONS

3.1. BLAST Observations

The seven nearby galaxies observed by BLAST were selected based on a number of competing criteria. First, the visibility requirements were restrictive, as they took into account BLAST's limited elevation range (25° – 60°), Sun and Moon avoidance criteria, and still had to make allowance for the changing latitude and longitude of the telescope arising from BLAST's uncertain ground path while aloft. Second, the galaxies had to be sufficiently large to be resolved by BLAST's optics (e.g. BLAST's $30''$ beam size at $250\,\mu\text{m}$ corresponds to 4 kpc at 25 Mpc). Third, they had to be sufficiently luminous for BLAST to be able to map them with a high SNR in the relatively small fraction of the flights scheduled for these observations. Finally, the sample needed to have measurements from the *Infrared Astronomical Satellite* (*IRAS*), the *Spitzer Space Telescope*, the Submillimeter Common-User Bolometer Array (SCUBA), or other experiments complementary to BLAST.

Table 1 summarizes relevant physical parameters of the BLAST nearby galaxy sample.¹⁵ The measured total flux in each BLAST band is tabulated in Table 2.

3.2. Other Multiwavelength Data

As part of the Spitzer Infrared Nearby Galaxies Survey (SINGS; Kennicutt et al. 2003), four of our sample (NGC 1097, NGC 1291, NGC 1512, and NGC 1566, hereafter BLAST/SINGS galaxies), have also been observed by the Multiband Imaging Photometer for Spitzer (MIPS) at $160\,\mu\text{m}$, $70\,\mu\text{m}$, and $24\,\mu\text{m}$ (Rieke et al. 2004) and the Infrared Array Camera (IRAC) at $8\,\mu\text{m}$, $6\,\mu\text{m}$, $4.5\,\mu\text{m}$, and $3.6\,\mu\text{m}$ (Fazio et al. 2004), both on the *Spitzer Space Telescope*. The remaining galaxies in our sample were not observed by *Spitzer*. Spatially integrated *Spitzer* fluxes are taken from Dale et al. (2007),

and MIPS maps used in this analysis come from the fifth SINGS public data release.¹⁶

IRAS data for all of our sample except NGC 1291 have been extracted from SCANPI.¹⁷ *IRAS* data for the fainter and more extended NGC 1291 are measured from HIRES generated maps (Aumann et al. 1990). These *IRAS* data are used, in addition to *Spitzer*, to constrain the spatially integrated SEDs of these galaxies. A 20% uncorrelated uncertainty is applied to all *IRAS* data. *IRAS* $25\,\mu\text{m}$ data are not used in this analysis when equivalent MIPS $24\,\mu\text{m}$ data are available.

Two of our sample have been observed by SCUBA: NGC 1097 at $850\,\mu\text{m}$ (Dale et al. 2005), and NGC 1808 at both 450 and $850\,\mu\text{m}$ (Stevens et al. 2005). These measurements do not cover the entire region of emission detected by BLAST. We omit these measurements from our analysis as a result. We exclude data from the *Infrared Space Observatory* (*ISO*) for NGC 1365 and NGC 4565 for similar reasons.

3.3. Individual Galaxies

A brief description of each observed galaxy follows.

3.3.1. NGC 1097

Features of NGC 1097, presented in Figure 1, include a bar 20 kpc in length that tapers off into two spiral arms (Beck et al. 2005), as well as several fringe structures called jets or ‘rays’ (Wolstencroft & Zealey 1975; Lorre 1978). NGC 1097 has an active Seyfert 1/LINER nucleus, which is considered to have a low-luminosity (Mason et al. 2007), and is surrounded by a $1.5\,\text{kpc}$ diameter nuclear ring, containing $1.1 \times 10^9\,\text{M}_\odot$ of molecular gas (Hsieh et al. 2008; Gerin et al. 1988). Thermal dust heating in the nuclear ring is dominated by a starburst (Mason et al. 2007) with a stellar production rate of $5\,\text{M}_\odot\,\text{yr}^{-1}$ (Hummel et al. 1987). BLAST made two observations of a $\sim 0.25\,\text{deg}^2$ area centered on NGC 1097, with a total integration time of 52 minutes. BLAST clearly resolves the bar and spiral arms of the galaxy, but has insufficient resolution to resolve the $1.5\,\text{kpc}$ star forming ring.

3.3.2. NGC 1291

NGC 1291, presented in Figure 2, is the brightest Sa galaxy in the Shapley-Ames Catalogue (Bregman et al. 1995). NGC 1291 has an orientation that is almost ‘face on’ and has a primary bar and secondary bar that have a 30° misalignment with each other (Pérez & Freeman 2006). The total H I mass is $2.4 \times 10^9\,\text{M}_\odot$, and there is little evidence for star formation in the central bulge (Hogg et al. 2001). BLAST made four observations of a $\sim 0.4\,\text{deg}^2$ area centered on NGC 1291, with a total integration time of 92 minutes. Although diffuse, BLAST detects both the central core of the galaxy, as well as the ring-like spiral structure $6'$ from the core.

3.3.3. NGC 1365

NGC 1365, presented in Figure 3, is usually classified as a Seyfert 1.5, but some authors list it as Seyfert 1

¹⁵ Instruction for obtaining BLAST maps used in this analysis may be found on <http://blastexperiment.info/>.

¹⁶ obtained from <http://data.spitzer.caltech.edu/popular/sings/>

¹⁷ available at <http://scanpi.ipac.caltech.edu:9000/applications/Scanpi>.

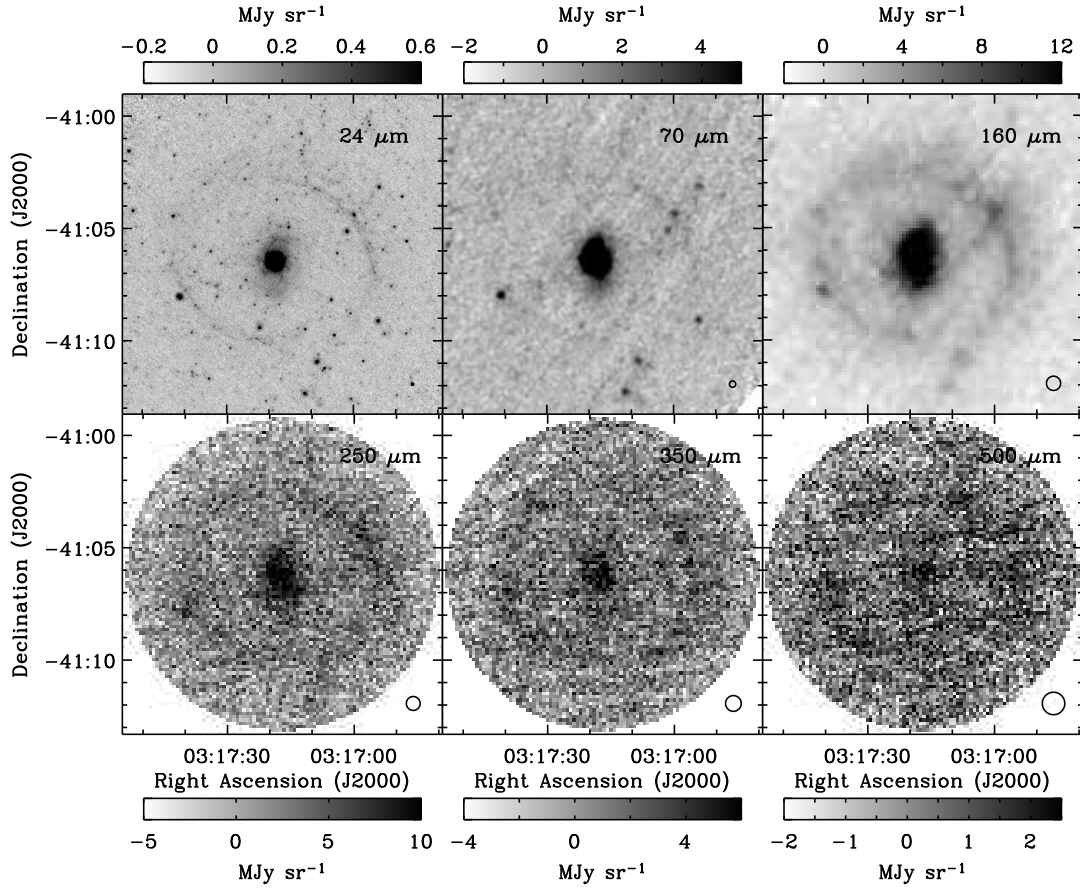


FIG. 2.— BLAST (*bottom row*) and MIPS (*top row*) observations of NGC 1291. The radius of the clipped map BLAST map is $7'$. The intensity scale is linear. The size of the BLAST and MIPS beams are plotted for reference in the lower right corner. The outer $6'$ ring of spiral arm structure is detected in all three BLAST bands, as is the central core.

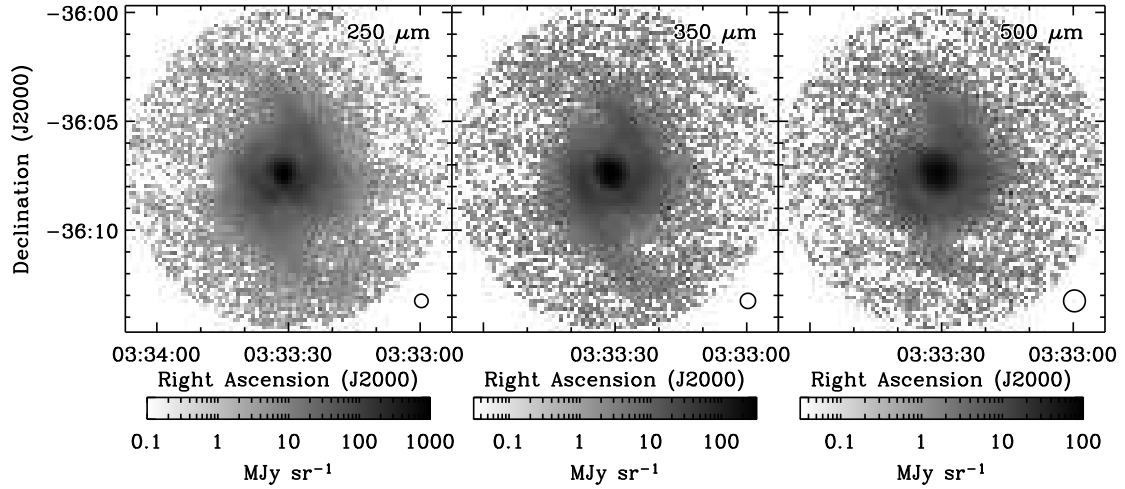


FIG. 3.— BLAST observations of NGC 1365. Pixels are $9''$ on a side. The radius of the clipped map is $6.5'$. Note the logarithmic intensity scale.

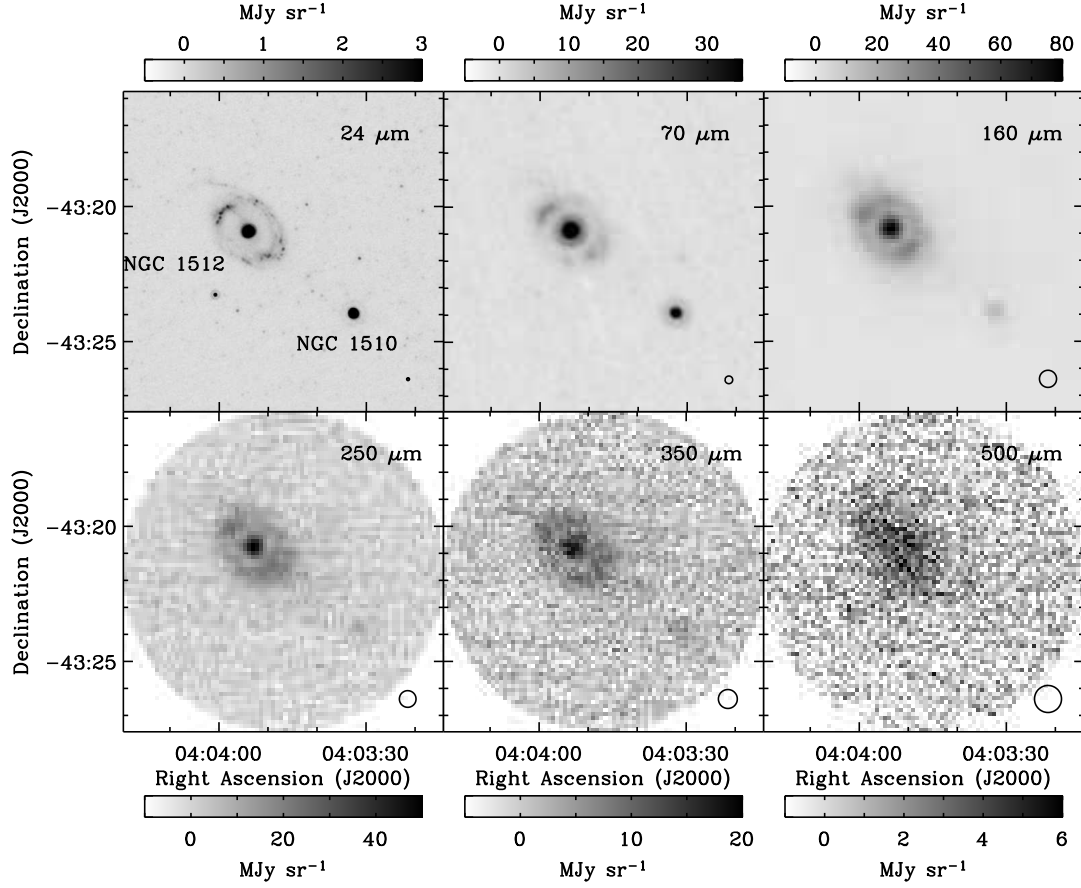


FIG. 4.— BLAST (*bottom row*) and MIPS (*top row*) observations of NGC 1512. The radius of the clipped BLAST maps is $6'$. The intensity scale is linear. The size of the BLAST and MIPS beams are plotted for reference in the lower right corner. BLAST detects the companion galaxy, NGC 1510 ($\alpha = 4^{\text{h}}03^{\text{m}}33^{\text{s}}$, $\delta = -43^{\circ}24'$; lower right) at $250\mu\text{m}$ and $350\mu\text{m}$. In these two bands, BLAST also can distinguish between the core and disc of NGC 1512.

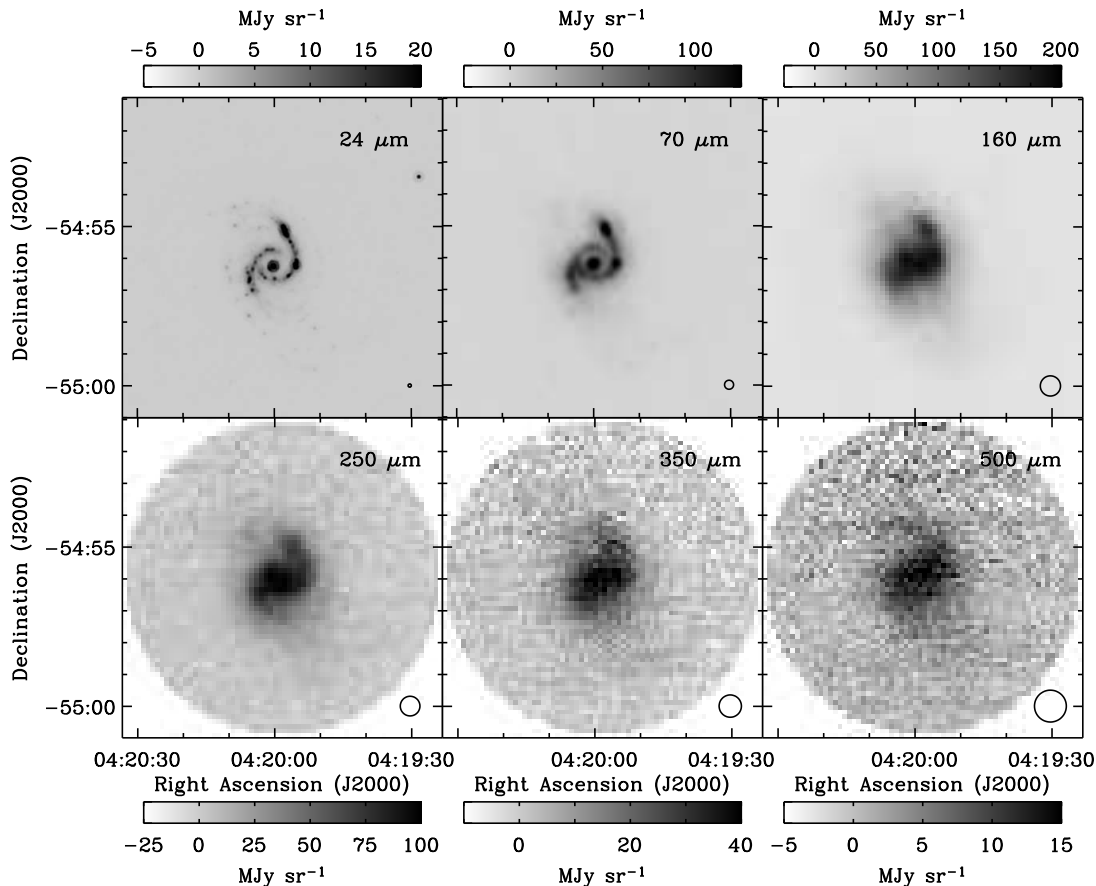


FIG. 5.— BLAST (bottom row) and MIPS (top row) observations of NGC 1566. The radius of the clipped BLAST maps is $5'$. The intensity scale is linear. The size of the BLAST and MIPS beams are plotted for reference in the lower right corner. BLAST detects the spiral arms, although the map is dominated by flux from the core.

or Seyfert 2 (e.g., Galliano et al. 2005; Véron et al. 1980; Alloin et al. 1981). The AGN has low luminosity, but there is evidence from optical studies to suggest that there is star formation surrounding the nucleus (Komossa & Schulz 1998). BLAST made three observations of a $\sim 0.25 \text{ deg}^2$ area centered on NGC 1365, with a total integration time of 30 minutes. The brightest of our sample, BLAST's observations prominently show both the bar and spiral arm structure of the galaxy.

3.3.4. NGC 1512

NGC 1512, presented in Figure 4, has a nucleus surrounded by a circumnuclear ring (Maoz et al. 2000). Beyond the ring, its spiral arms are complicated by its satellite galaxy, NGC 1510 (Kinman 1978). BLAST made three observations of a $\sim 0.45 \text{ deg}^2$ area centered on NGC 1512, with a total integration time of 28 minutes. BLAST detects the core and tightly wound central spiral of NGC 1512. BLAST also detects the companion galaxy, NGC 1510.

3.3.5. NGC 1566

NGC 1566, presented in Figure 5, is the second brightest known Seyfert galaxy (de Vaucouleurs 1973). Extending from the nucleus are two prominent spiral arms which continue outward to form the galaxy's outer ring that is at an inclination of about 30° (Bottema 1992; de Vaucouleurs 1975). The arms contain a significant

amount of star formation (Bottema 1992). BLAST made two observations of a $\sim 0.7 \text{ deg}^2$ area centered on NGC 1566, with a total integration time of 50 minutes. BLAST resolves the spiral structure of the galaxy, and the observations are dominated by submillimeter flux originating in the core of the galaxy.

3.3.6. NGC 1808

NGC 1808, presented in Figure 6, is a Seyfert 2 galaxy (Jiménez-Bailón et al. 2005). Subsequent measurement seems to indicate that a large part of the radiation emanating from the central 1 kpc of the galaxy is from an active galactic nucleus as well as a high rate of star formation (Förster Schreiber et al. 2003; Maiolino et al. 2003). Using *ROSAT*, Junkes et al. (1995) estimate a star formation rate of between 5 and $13 \text{ M}_\odot \text{ yr}^{-1}$, and a supernova event rate of 0.09 yr^{-1} . A companion galaxy, not observed by BLAST, NGC 1792 is located $40'$ from NGC 1808 (130 kpc at a distance of 10.9 Mpc) and may be responsible for an accelerated star formation rate in NGC 1808 (Jiménez-Bailón et al. 2005). BLAST made four observations of a $\sim 1 \text{ deg}^2$ area centered on NGC 1808, with a total integration time of 179 minutes. BLAST detects both the core and disc of the galaxy. BLAST also detects excess flux in this map near the location of the interacting galaxies ESO 305-IG 010 ($\alpha = 5^{\text{h}}08^{\text{m}}27^{\text{s}}$, $\delta = -37^\circ39'5''$, $z = 0.0524$).

3.3.7. NGC 4565

NGC 4565, presented in Figure 7, is an edge-on barred-spiral galaxy in the constellation Coma Berenices. It has an apparent size of about $12' \times 2.5'$. Although degraded by the large point-spread functions of BLAST05 (186–189", Truch et al. 2008), NGC 4565 is still resolved by BLAST. BLAST made one observation of a $\sim 0.4 \text{ deg}^2$ area centered on NGC 4565, with a total integration time of 49 minutes. A beam-deconvolved image, using the method described in §2.4 of Chapin et al. (2008), is shown in the bottom row of Figure 7.

We fit an exponential profile to the beam-deconvolved maps of the form $\exp(|x|/s)$, where x is a spatial variable aligned along the major axis of the galactic disk and s is the scale length, and find scale lengths of 118", 156", and 142" at 250 μm , 350 μm , and 500 μm , respectively. The 250 μm fit, which has the highest signal-to-noise ratio, agrees well with scale lengths measured at other wavelengths (e.g., van der Kruit & Searle 1981; Rice et al. 1996; Engargiola & Harper 1992). In this fit we have ignored the central $3'$ region of the galaxy. This region corresponds to an area of reduced 250 μm flux, possibly corresponding to the molecular ring seen in ^{12}CO (Neininger et al. 1996).

4. SED FITTING

4.1. Physical Dust Models

For the four BLAST/SINGS galaxies, we fit the silicate-graphite-PAH dust models of Draine & Li (2007), hereafter *DL07*, to BLAST, MIPS, *IRAS*, and IRAC data. These models have already been applied, without the benefit of BLAST observations, to the same galaxies in Draine et al. (2007), hereafter *Dr07*. We independently recreate this analysis with the inclusion of the BLAST data. These models provide the dust emissivity per hydrogen atom, $j_\nu(q_{\text{PAH}}, U_{\text{min}}, U_{\text{max}})$, dependent on three model parameters:

1. q_{PAH} , the fraction of total dust mass in polycyclic aromatic hydrocarbons (PAHs) containing less than 10^3 carbon atoms;
2. U_{min} , a starlight intensity factor characterizing the radiation field heating the diffuse ISM;
3. U_{max} , a starlight intensity factor characterizing the radiation field in more intense star forming regions, including photodissociative regions (PDRs).

Both U_{min} and U_{max} are relative to the specific energy density of starlight measured by Mathis et al. (1983). *Dr07* consider a fourth model parameter, α , which is the exponent characterizing the power-law decrease in starlight intensity: $dM_d/dU \propto U^{-\alpha}$. They find the model fits to be insensitive to its value, and the models provided have $\alpha = 2$.

Our fitting procedure follows that of *Dr07*. We restrict ourselves to the seven Milky Way dust model sets¹⁸ (Weingartner & Draine 2001, updated by *DL07*). These seven model sets have values of q_{PAH} between 0.47% and 4.6%. We take linear combinations of these to produce 43 different model sets for a finer-grained sampling of q_{PAH} .

Each set contains values of j_ν for twenty-two values of U_{min} between 0.1 and 25, and for five “PDR models” with values of U_{max} (10^2 , 10^3 , 10^4 , 10^5 , 10^6), plus one “diffuse ISM model” with $U_{\text{max}} = U_{\text{min}}$.

These dust models are combined with a stellar blackbody to produce a galactic model:

$$F_{\nu, \text{model}} = \Omega_\star B_\nu(T_\star) + \frac{M_d}{m_H D^2} \left(\frac{M_H}{M_d} \right) \times [(1 - \gamma) j_\nu(q_{\text{PAH}}, U_{\text{min}}, U_{\text{min}}) + \gamma j_\nu(q_{\text{PAH}}, U_{\text{min}}, U_{\text{max}})] \quad (1)$$

where Ω_\star is the solid angle subtended by stars, $B_\nu(T)$ is the Planck function, the nominal stellar temperature $T_\star = 5000 \text{ K}$, M_d is the total dust mass, m_H the mass of a hydrogen atom, D the distance to the galaxy, and γ a mixing fraction between the diffuse ISM ($U_{\text{max}} = U_{\text{min}}$) and PDR ($U_{\text{max}} > U_{\text{min}}$) dust models. The hydrogen-to-dust mass ratio, M_H/M_d , is set by the model choice, and varies from 96 to 100.

Like *Dr07*, we find that the best fits for the four galaxies are insensitive to the choice of U_{max} , and so set $U_{\text{max}} = 10^6$. We obtain the best-fit values of Ω_\star , M_d , γ , q_{PAH} , and U_{min} through χ^2 minimization (see §4.5).

The best-fit models for the galaxies to the extended *Spitzer-IRAS*-BLAST data set are plotted in Figure 8. This figure also plots the spatially integrated *Spitzer* and *IRAS*, BLAST, and SCUBA measurements for these galaxies.

The model parameters are tabulated in Table 3. We also tabulate the dust-weighted mean starlight intensity scale factor

$$\langle U \rangle = \left[(1 - \gamma) U_{\text{min}} + \gamma \frac{\ln(U_{\text{max}}/U_{\text{min}})}{U_{\text{min}}^{-1} - U_{\text{max}}^{-1}} \right] \quad (2)$$

and the dust luminosity calculated from the model fit.

4.2. Modified Blackbody SEDs

In addition to the *DL07* models, we also fit BLAST plus available MIPS 70 and 160 μm and *IRAS* 100 μm data to a single-component modified blackbody SED:

$$F_{\nu, \text{model}} = \frac{M_d \kappa}{D^2} \left(\frac{\nu}{\nu_0} \right)^\beta B_\nu(T) \quad (3)$$

where the dust emissivity index, β , is fixed to 2, and ν_0 to 1.2 THz = $c/250 \mu\text{m}$. An uncertainty of $\pm 0.3 \text{ Mpc}$ is assumed for all galaxy distances.

The dust mass absorption co-efficient at ν_0 , κ , is not well determined, and depends on the object investigated (see Netterfield et al. 2009 for a discussion). For each BLAST/SINGS galaxy, we calculate a value for κ by comparing the *DL07* fit to the fit found for the spatially integrated modified blackbody SED (§4.3). The values of κ for each galaxy are summarized in Table 3. These values are used in the calculation of the column density maps presented in Figure 11. For the galaxies without *Spitzer* observations, we use the mean value, $\kappa = 0.29 \pm 0.03 \text{ m}^2 \text{ kg}^{-1}$, to calculate dust mass from the modified blackbody fits.

For each fit, a brute-force grid search is performed to simultaneously fit M_d and T to the data. The temperature, T , is sampled at 1000 uniformly-spaced points between 5 K and 30 K. This range was determined by first

¹⁸ obtained from <http://www.astro.princeton.edu/~draine/dust/dustmodels.html>

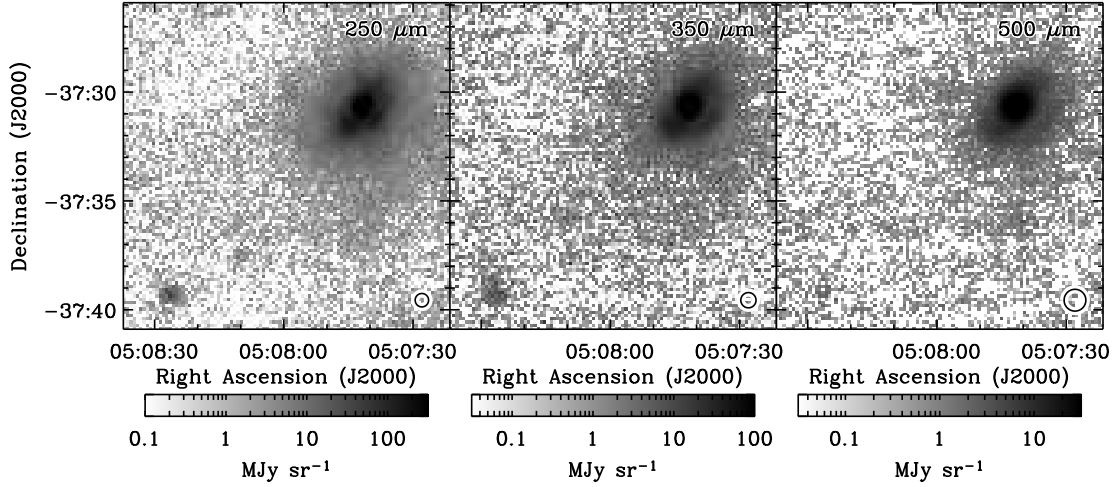


FIG. 6.— BLAST observations of NGC 1808 (upper right). Pixels are $9''$ on a side. BLAST also detects excess flux near the position of the interacting galaxies ESO 305-IG 010 ($\alpha = 5^{\text{h}}08^{\text{m}}27^{\text{s}}$, $\delta = -37^{\circ}39'5$, $z = 0.0524$; lower left). Note the logarithmic intensity scale.

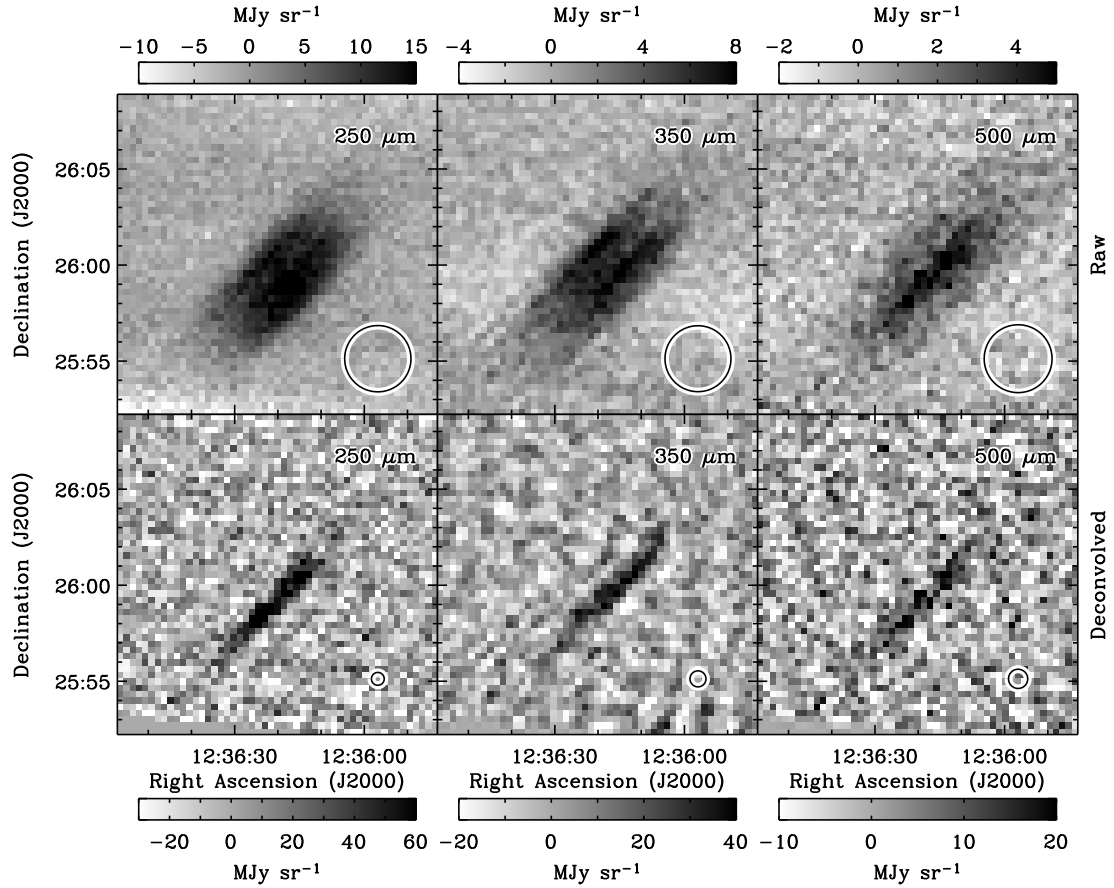


FIG. 7.— *Top row*: BLAST observations of NGC 4565. *Bottom row*: Results of deconvolving the raw maps following the procedure outlined in §2.4 of Chapin et al. (2008). This deconvolution process results in 3–5 times better resolution, at a cost of reduction in signal-to-noise of a factor of ~ 2 . Pixels are $20''$ on a side. Note the linear intensity scale. Effective beam sizes, based on the full widths at half-power (FWHP) found in Table 1 of Chapin et al. (2008), are plotted in the lower right corners for both the raw and deconvolved maps. The full BLAST05 point spread functions are shown in Figure 1 of Truch et al. (2008).

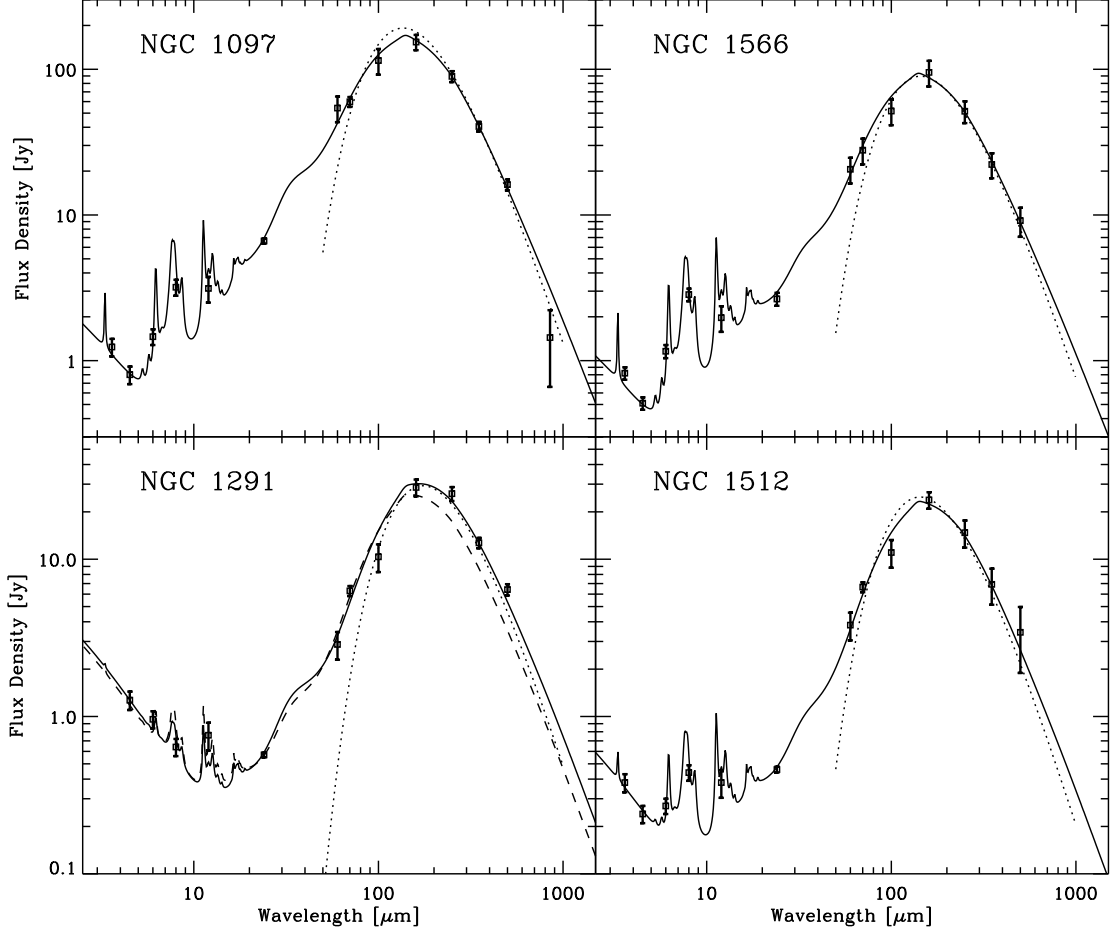


FIG. 8.— Spatially integrated SEDs for the four galaxies in the SINGS sample. Data shown are from BLAST, MIPS, IRAC, and *IRAS*. The SCUBA 850 μm measurement of NGC 1097 (Dale et al. 2005) is also shown, but not included in this analysis. The solid curves are the best-fit physical dust models of Draine & Li (2007) (*DL07*; see § 4.1) fit in this analysis to *Spitzer*, *IRAS* and BLAST. The dashed curve in the panel for NGC 1291 is the best-fit *DL07* model subject to the constraint $U_{\text{min}} \geq 0.7$. The dotted curves are the best-fit single-component modified blackbody model (§ 4.3). Parameters for these fits are summarized in Tables 2 and 3.

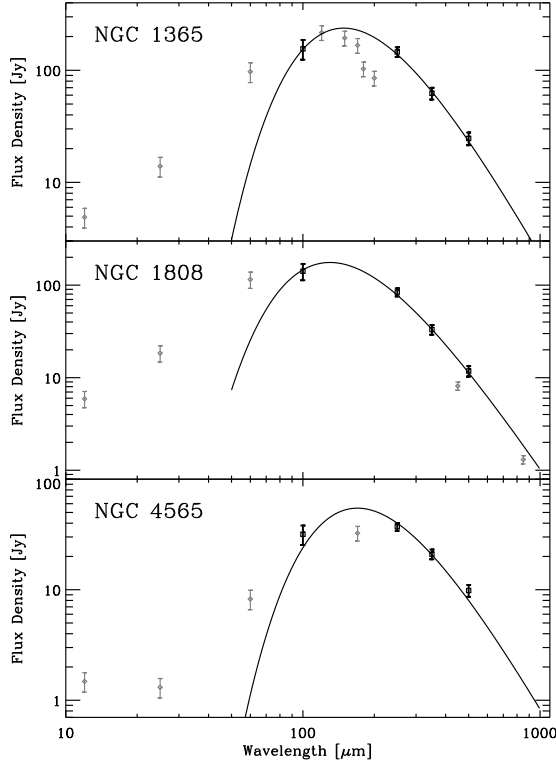


FIG. 9.— Spatially integrated SEDs for the three galaxies not in the SINGS sample. Modified blackbody fits to BLAST plus *IRAS* 100 μm are shown. Other data, which were not included in the fit, from SCUBA (Stevens et al. 2005), *ISO* (Spinoglio et al. 2002; Stickel et al. 2004) and *IRAS* are the lighter diamonds. Masses and temperatures from these fits are presented in Table 2.

letting temperatures vary over a much wider range (1 K–100 K) and then discarding those portions of the phase space discovered to be irrelevant to the fitting procedure. Because the dust mass, M_d , may vary by several orders of magnitude, the sampling limits for the dust mass are automatically adjusted as necessary for the fit, and sampled uniformly at 1000 points. As with the DL07 models, goodness-of-fit is assessed using a χ^2 test (§ 4.5). The marginalized likelihood is used to determine medians and 68% confidence intervals for the two fit parameters.

4.3. Spatially Integrated SED Fits

For the three galaxies without *Spitzer* data, we fit Equation 3 to BLAST plus *IRAS* 100 μm . The *IRAS* and BLAST measurements used to constrain the fits, and the results from these fits are presented in Figure 9, which also plots additional data from *IRAS*, *ISO* and SCUBA, not used in this analysis.

For the four BLAST/SINGS galaxies, we also fit Equation 3 to BLAST, plus 160, 100, and 70 μm data from MIPS or *IRAS*, to compare with the results of the DL07 models. These fits are plotted in Figure 8 as dotted curves. We note reasonably good agreement between the two models for all galaxies near the thermal peak. On the Wien side of the peak, the modified blackbody quickly falls off in comparison to the DL07 model fit. On the Rayleigh-Jeans side, the modified blackbody also falls off faster than the DL07 model fit. For NGC 1097 and NGC 1291, the modified blackbody underpredicts the 500 μm flux by more than 1- σ .

Dust temperatures from these fits for all galaxies in the

sample are listed in Table 2, as are dust masses for the three galaxies without *Spitzer* observations.

4.4. Subgalactic SED Fits

Because the MIPS beams at 70 μm and 160 μm are of comparable size to the BLAST beams, we also investigate the dust properties on sub-galactic scales for the four BLAST/SINGS galaxies. To do this, the BLAST maps produced for the four galaxies were made on the same 9'' pixel grid as the the MIPS 160 μm maps. The 70 μm MIPS images, which have a compatibly aligned 4.5 pixel grid, are rebinned to 9'' to put them on the same grid. All five maps are then convolved (smoothed) to the resolution of the 500 μm data (60'') and our modified blackbody template (Equation 3) is fit to the data at each pixel in the map.

The central twelve pixels of NGC 1097 have 70 μm flux in excess of 200 MJyr $^{-1}$. For these pixels, the 70 μm data are excluded, due to possible non-linearities,¹⁹ and the model is fit to four photometric points only.

Resultant temperature and column density maps for the four galaxies are presented in Figures 10 and 11. NGC 1510, the companion galaxy to NGC 1512, appears quite prominently in these maps as seemingly hotter (>25 K) than NGC 1512. This is not believed to be a real effect, and is likely due to poor performance by the fitting routine on the data for NGC 1510, for which $\beta = 2$ is probably not an appropriate choice.

Radially-averaged temperature and column density profiles are plotted in Figure 12. We note a general decrease in both column density and dust temperature with increasing radius. Of the four galaxies, we notice two subgroups of two galaxies each. The brighter NGC 1097 and NGC 1566, for which BLAST detects high intensity emission continuously from the core to disc of the galaxy, have relatively flat temperature profiles. NGC 1291 and NGC 1512, which BLAST detects with a more isolated core, fall off more steeply. We also potentially detect the 1.5 kpc star-forming ring in NGC 1097, which causes the kink in the temperature profile.

4.5. χ^2 Calculation

We use χ^2 minimization to assess goodness of fit for both the DL07 models and the modified blackbody model. The BLAST calibration uncertainties are highly correlated between observational bands (Truch et al. 2008, 2009). Given observational data, s_d , and band-convolved model predictions, \tilde{s} , we compute

$$\chi^2 \equiv (\tilde{s} - s_d)^T C^{-1} (\tilde{s} - s_d) \quad (4)$$

where C^{-1} is the inverse data covariance matrix, and $(\cdot)^T$ denotes the transpose. Given the the calibration uncertainty correlation matrix, ρ , the data covariance matrix is:

$$C_{ij} = \delta_{ij} [(\sigma_d^2)_i + (\sigma_m^2)_i] + \rho_{ij} (\sigma_c)_i (\sigma_c)_j \quad (5)$$

where σ_d is the measurement uncertainty, σ_c the calibration uncertainty, and σ_m an uncertainty associated with the model. For the DL07 models, in order to compare with their results, we follow Dr07 and adopt $\sigma_m = 0.1s_d$.

¹⁹ http://data.spitzer.caltech.edu/popular/sings/20070410_enhanced_v

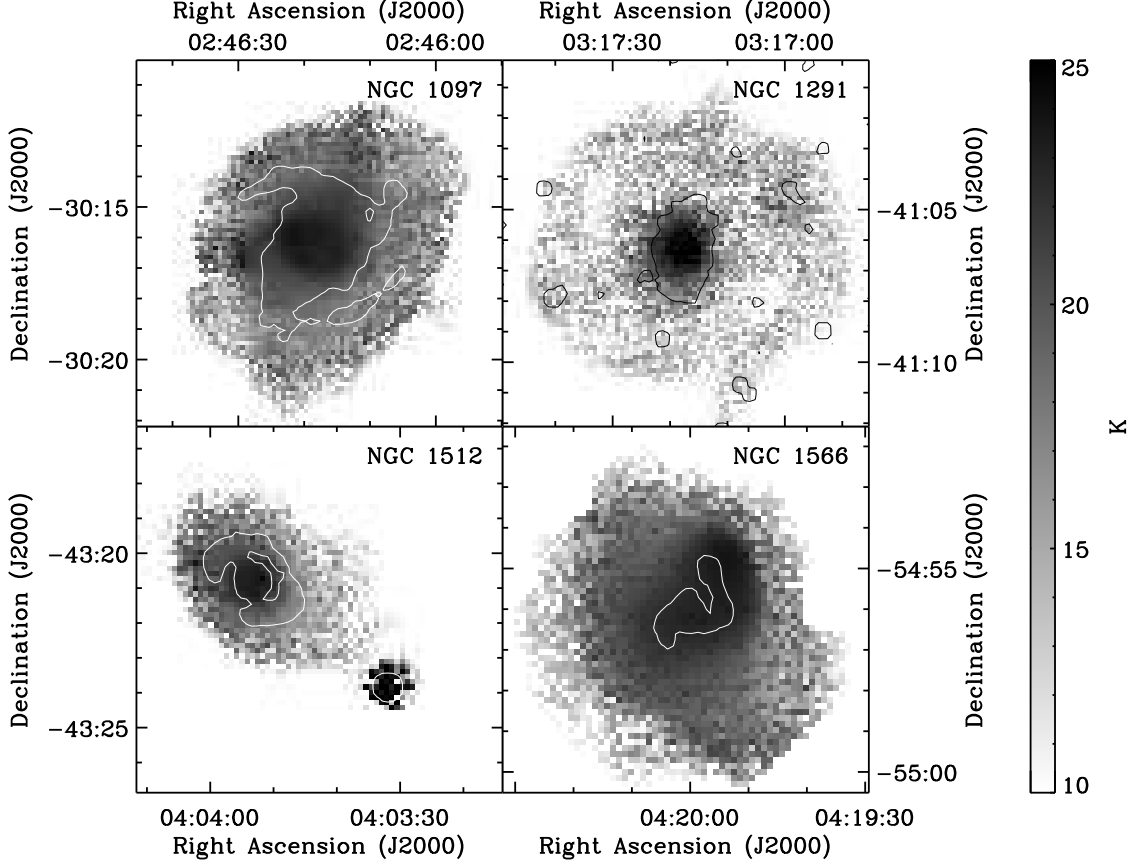


FIG. 10.— Dust temperature maps based on BLAST and MIPS observations for the four BLAST/SINGS galaxies. Only those pixels whose $250\text{ }\mu\text{m}$ flux is inconsistent with zero at the $1\text{-}\sigma$ level are plotted. Contours from the $24\text{ }\mu\text{m}$ MIPS maps, smoothed with a $18''\times 18''$ window function, are overplotted for comparison. For NGC 1097 and NGC 1512, the 0.3 MJy sr^{-1} $24\text{-}\mu\text{m}$ contour is plotted. For NGC 1291, the 0.1 MJy sr^{-1} contour is used, and for NGC 1566, the 5 MJy sr^{-1} contour is plotted.

For the modified blackbody model, we use $\sigma_m = 0$. We assume that *IRAS* and *Spitzer* uncertainties are uncorrelated between bands, and set $\rho_{ij} = \delta_{ij}$ for non-BLAST measurements.

For the BLAST measurements, we set ρ to the value of the Pearson correlation matrices computed as outlined in Truch et al. (2008, 2009). For both the calibration uncertainty (σ_c) and the calibration uncertainty correlation matrix (ρ), we add to the values given in those papers an additional source of uncertainty associated with our ability to measure the BLAST bandpasses. We estimate the error in the bandpass measurements to be at most 5%. We additionally assume that this uncertainty is uncorrelated between bands.

The magnitude of the effect of bandpass measurement error on the BLAST calibration uncertainties depends on the spectrum of the object observed. A source with same spectrum as our calibrator (VY Canis Majoris, for which Truch et al. (2009) find a best-fit single-component modified blackbody with $T = 346 \pm 19\text{ K}$ and $\beta = 0.55 \pm 0.05$) is unaffected by bandpass errors, but for a source with a significantly different spectrum, the effect can be non-negligible, especially in the high SNR case. This is the case in this study, and we have adjusted our calibration uncertainties accordingly.

Because the underlying spectrum of the galaxies is unknown, we use the modified blackbody model as a proxy. The calculated calibration uncertainties affect the best

fit of the model, so this is an iterative process: we first fit the model using a guess for the calibration uncertainties, and then update the uncertainties based on the best fit. This process is iterated until convergence is achieved. In general only one iteration after the initial guess is required for convergence.

For this operation, we have calculated calibration uncertainties and uncertainty correlations for various $\beta = 2$ modified greybody models with temperatures in the range 15–25 K. The resulting calibration uncertainties vary most with choice of model at $250\text{ }\mu\text{m}$ (12–14% for BLAST06), with smaller variations at $350\text{ }\mu\text{m}$ (10.0–10.5%) and $500\text{ }\mu\text{m}$ (8.00–8.25%). The uncertainty correlations calculated show similar behavior, varying between 0.80 and 0.97 for the $250\text{--}350\text{ }\mu\text{m}$ correlation to but only 0.91–0.92 for the $350\text{--}500\text{ }\mu\text{m}$ correlation.

When reporting goodness of fit, we report χ^2 per degree of freedom:

$$\chi_r^2 \equiv \frac{1}{N_b - N_m} \chi^2 \quad (6)$$

where N_b is the number of observational bands considered in the fit, and N_m the number of model parameters (five for the DL07 models and two for the modified blackbody model). The number of bands ranges from four (3 BLAST + $100\text{ }\mu\text{m}$ *IRAS*) for modified blackbody fits in the absence of *Spitzer* data, to thirteen (4 IRAC, 3 *IRAS*, 3 MIPS, 3 BLAST) when fitting the DL07 mod-

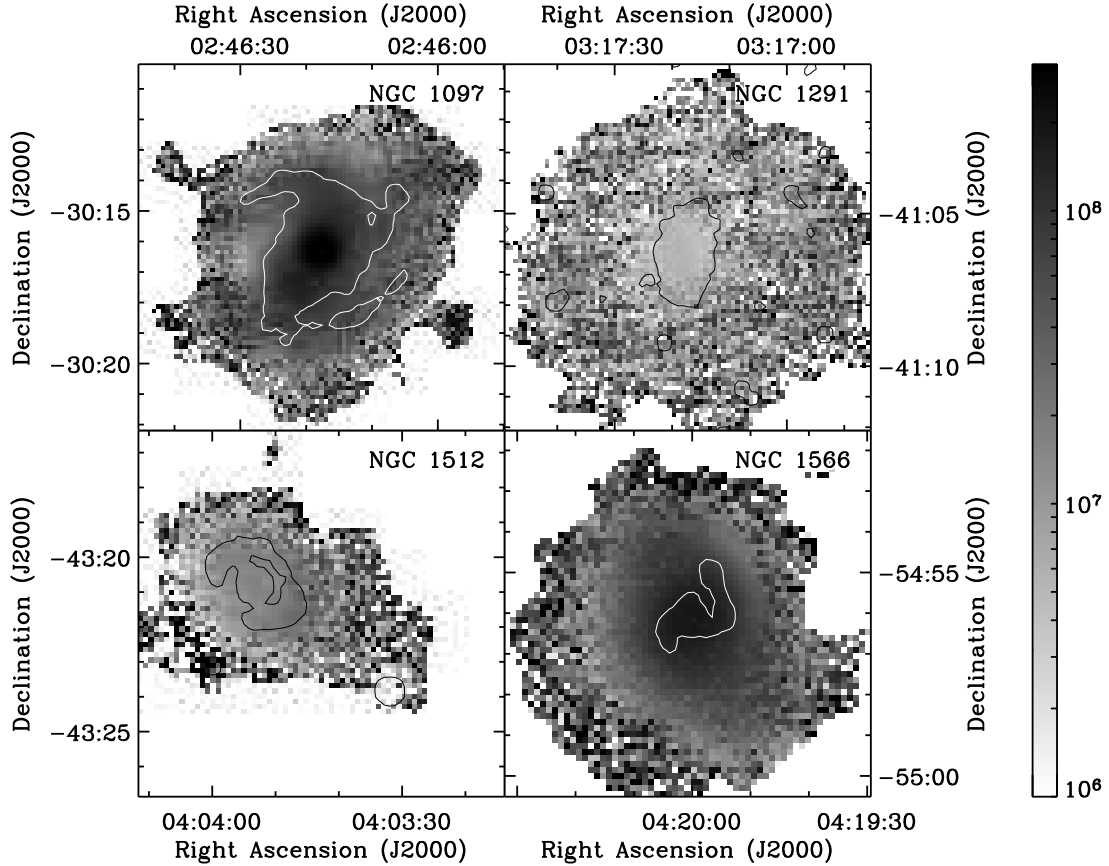


FIG. 11.— Dust column density maps based on BLAST and MIPS observations for the four BLAST/SINGS galaxies. Only those pixels whose $250\ \mu\text{m}$ flux is inconsistent with zero at the $1\text{-}\sigma$ level are plotted. Contours plotted are the same as in Figure 10.

els.

5. DISCUSSION

5.1. Physical Dust Models

Of the four galaxies observed by both BLAST and *Spitzer*, the DL07 fits we find for all but NGC 1291 are consistent with the best-fit models determined without BLAST data in Dr07. For NGC 1291 we find a dust mass approximately two times larger than Dr07. This discrepancy is due to the restriction $U_{\min} \geq 0.7$ imposed by Dr07 in the absence of SCUBA data. We fore-go this restriction for our fit of NGC 1291, and find a best-fit $U_{\min} = 0.2$. Constraining $U_{\min} \geq 0.7$ results in a fit consistent with that of Dr07 ($q_{\text{PAH}}=2.8\%$, $U_{\min}=0.7$, $\log(M_d/M_\odot)=7.36$, $\gamma = 1.00\%$), but a poor fit to BLAST data ($\chi_r^2 = 2.59$). This fit is plotted in Figure 8 for comparison.

5.2. Galaxy Colors

The high SNR BLAST measurements in Table 2 strongly constrains the shape of the galactic SEDs. Using this shape information, we can attempt to determine T and β for the single-component modified blackbody model (Equation 3) directly. All seven galaxies in our sample are plotted on a color-color plot in Figure 13. Also plotted are various isotherms and isobeta contours. This single-component modified blackbody model is clearly inconsistent, regardless of choice of β , with at least some of these high signal-to-noise data,

which is not surprising given the simplicity of the model.

5.3. Fraction of Core to Total Emission

BLAST's unique ability to spatially map the submillimeter flux of this sample fully, along with its resolution, allow us to investigate the fraction of submillimeter flux which arises from the central core of these galaxies. Although BLAST's resolution is insufficient to resolve the central AGN of these galaxies (where present), we can put limits on the contribution made to the submillimeter flux by active galactic nuclei. This is important for the determination of star formation rates from submillimeter observation of distant galaxies (e.g., Devlin et al. 2009).

For each galaxy, except the edge-on NGC 4565, we find the 3 db point of the $250\ \mu\text{m}$ radial flux contour and use this radius to define the core of the galaxy. Fluxes in all three BLAST bands from this core region are presented in Table 4. Also in this table is the “core fraction,” the fraction of the total BLAST measured flux which originates in the core of the galaxy.

Most of the sample have core fractions in the range 7.5% to 15%. NGC 1566 is a clear outlier, with roughly a third of the submillimeter flux in the core of the galaxy. The second brightest known Seyfert galaxy (de Vaucouleurs 1973), NGC 1566 has a core whose submillimeter flux originates largely from the AGN. The galaxy with the smallest core fraction is NGC 1291, a galaxy with no known active nucleus.

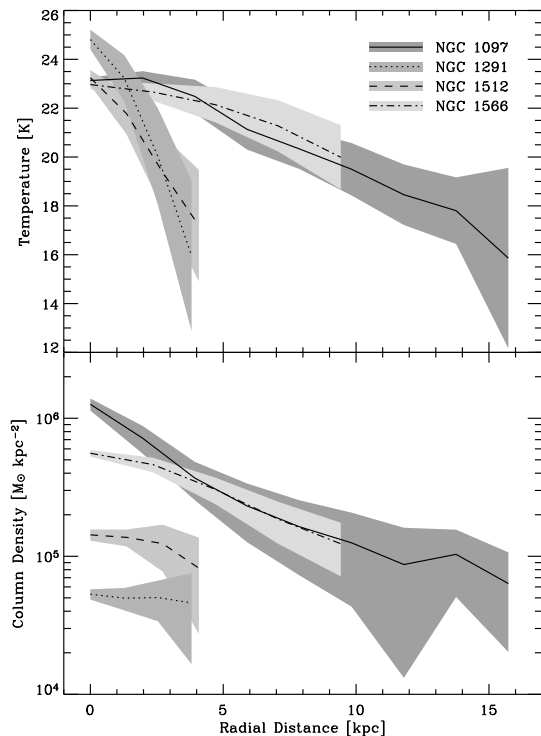


FIG. 12.— Mean radial dust temperature (top) and dust column density (bottom) for the four BLAST/SINGS galaxies, with $1\text{-}\sigma$ uncertainty bands. Resolution elements at $500\text{ }\mu\text{m}$ are approximately 4.9, 5.2, 3.0, and 2.8 kpc for NGC 1097, NGC 1291, NGC 1512, and NGC 1566, respectively.

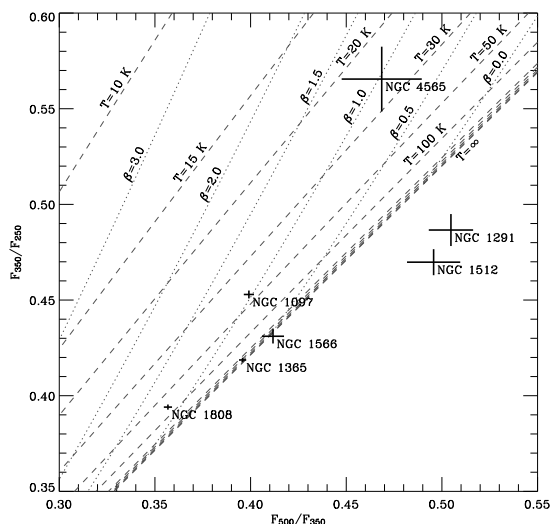


FIG. 13.— Color-color plot of the seven BLAST galaxies. Crosses indicate $1\text{-}\sigma$ errors, assuming the BLAST calibration uncertainty is 100% correlated. Contours of both constant T varying β and constant β varying T from the modified blackbody model (eq. 3) are also shown. The model is clearly inconsistent with some of the data.

All galaxies show a decrease in core fraction with increasing wavelength, a result of the core dust temperature being generally warmer than the dust in the surrounding disc (see Figure 12). Other than NGC 1566, most galaxies have weak or no AGN, although BLAST is unable to separate AGN derived flux from star formation in the central regions of the galaxies. In the case of NGC 1097, the unresolved $18''$ circumnuclear starburst ring (e.g., Hummel et al. 1987; Barth et al. 1995; Quillen et al. 1995; Kotilainen et al. 2000), likely provides a sizable contribution to the total core flux.

A simple model based on the mean flux of the disk of the galaxies and the mean flux of NGC 1291 indicates that approximately 5% of the submillimeter luminosity of LIRGS and ULIRGS comes from star formation driven heating in the core. In many galaxies, an excess of 2.5–10% (and as high as 25%) appears to come from AGN-driven flux. The result leads to a significant overestimate of star formation in galaxies with AGN, unless this effect can be taken into account.

6. SUMMARY

BLAST made resolved observations of seven nearby galaxies over the course of two flights. Four of these galaxies, NGC 1097, NGC 1291, NGC 1512, and NGC 1566, have complementary *Spitzer* observations as part of the SINGS survey. For these four galaxies, we fit the models of Draine & Li (2007) to BLAST, *Spitzer*, and *IRAS* observations. Best-fit parameters are tabulated in Table 3.

The best-fit models for three of these four galaxies are consistent with the best-fit models calculated in Draine et al. (2007) without BLAST data. For the fourth galaxy, NGC 1291, we find a dust mass roughly two times larger than the dust mass determined by Draine et al. (2007). We also calculate a value for the dust mass absorption coefficient at $250\text{ }\mu\text{m}$ $\kappa = 0.29 \pm 0.03\text{ m}^2\text{ kg}^{-1}$ by comparing the Draine & Li models with a modified blackbody model.

For these four galaxies, we also produce maps of dust column density and mean dust temperature based on BLAST and MIPS observations fit to a single component modified blackbody model (Figures 10 and 11), as well as radial profiles of the same quantities (Figure 12).

For the remaining three galaxies observed by BLAST but not observed by *Spitzer*, NGC 1365, NGC 1808, and NGC 4565, we calculate spatially integrated dust temperatures and dust masses by fitting a modified blackbody model to BLAST and *IRAS* data. Results are summarized in Table 2.

We calculate the fraction of the submillimeter detected flux originating in the core of the galaxy as a fraction of the total submillimeter emission from the galaxy. Although BLAST is unable to resolve the nucleus of these galaxies, the ratio of compact to extended flux measured by BLAST puts an important upper limit on the fraction of submillimeter radiation driven by a central AGN. We find in the AGN-quiet NGC 1291, approximately 5% of the total BLAST detected flux arises in the core. In much of our sample, core fraction is 8% or higher. In the extreme case of NGC 1365, the second brightest known Seyfert galaxy, a third of the submillimeter flux originates in the core. In general the core fraction increases with decreasing wavelength, indicating that dust in the

core of these galaxies is warmer than the dust in the surrounding disc.

For NGC 4565, we calculate a scale length of $118''$, $156''$, $142''$ at $250\mu\text{m}$, $350\mu\text{m}$, and $500\mu\text{m}$, respectively, in good agreement with measurements at other wavelengths.

The BLAST collaboration acknowledges the support of NASA through grant numbers NAG5-12785, NAG5-13301, and NNGO-6G111G, the Canadian Space Agency (CSA), Canada's Natural Sciences and Engineering Research Council (NSERC), and the UK Particle Physics & Astronomy Research Council (PPARC). We would also like to thank the Columbia Scientific Balloon Facility (CSBF) staff for their outstanding work. LO acknowl-

edges partial support by the Puerto Rico Space Grant Consortium and by the Fondo Institucional para la Investigación of the University of Puerto Rico. CBN acknowledges support from the Canadian Institute for Advanced Research. This research has been enabled by the use of WestGrid computing resources.

This work is based in part on observations made with the *Spitzer Space Telescope*, and has also made use of the NASA/IPAC Extragalactic Database (NED), both of which are operated by the Jet Propulsion Laboratory, California Institute of Technology, under contracts with the National Aeronautics and Space Administration. This research also made use of the SIMBAD database, operated at the Centre de Données astronomiques de Strasbourg (CDS), Strasbourg, France.

REFERENCES

- Alloin, D., Edmunds, M. G., Lindblad, P. O., & Pagel, B. E. J. 1981, *A&A*, 101, 377
- Aumann, H. H., Fowler, J. W., & Melnyk, M. 1990, *AJ*, 99, 1674
- Barth, A. J., Ho, L. C., Filippenko, A. V., & Sargent, W. L. 1995, *AJ*, 110, 1009
- Beck, R., Fletcher, A., Shukurov, A., Snodin, A., Sokoloff, D. D., Ehle, M., Moss, D., & Shoutenkov, V. 2005, *A&A*, 444, 739
- Boselli, A., et al. 2008, in SF2A-2008, ed. C. Charbonnel, F. Combes, & R. Samadi, 361
- Bottrema, R. 1992, *A&A*, 257, 69
- Bregman, J. N., Hogg, D. E., & Roberts, M. S. 1995, *ApJ*, 441, 561
- Chapin, E. L., et al. 2008, *ApJ*, 681, 428
- Dale, D. A., et al. 2005, *ApJ*, 633, 857
- . 2007, *ApJ*, 655, 863
- de Vaucouleurs, G. 1973, *ApJ*, 181, 31
- . 1975, *ApJS*, 29, 193
- de Vaucouleurs, G., de Vaucouleurs, A., Corwin, Jr., H. G., Buta, R. J., Paturel, G., & Fouque, P. 1991, Third Reference Catalogue of Bright Galaxies
- Devlin, M., et al. 2009, *Nature*, 458, 737
- Draine, B. T., et al. 2007, *ApJ*, 663, 866
- Draine, B. T., & Li, A. 2007, *ApJ*, 657, 810
- Engargiola, G., & Harper, D. A. 1992, *ApJ*, 394, 104
- Fazio, G. G., et al. 2004, *ApJS*, 154, 10
- Fixsen, D. J., Dwek, E., Mather, J. C., Bennett, C. L., & Shafer, R. A. 1998, *ApJ*, 508, 123
- Förster Schreiber, N. M., Sauvage, M., Charmandaris, V., Laurent, O., Gallais, P., Mirabel, I. F., & Vigroux, L. 2003, *A&A*, 399, 833
- Galliano, E., Alloin, D., Pantin, E., Lagage, P. O., & Marco, O. 2005, *A&A*, 438, 803
- Gerin, M., Combes, F., & Nakai, N. 1988, *A&A*, 203, 44
- Griffin, M., et al. 2007, *Advances in Space Research*, 40, 612
- Hogg, D. E., Roberts, M. S., Bregman, J. N., & Haynes, M. P. 2001, *AJ*, 121, 1336
- Holland, W. S., et al. 1999, *MNRAS*, 303, 659
- Hsieh, P.-Y., Matsushita, S., Lim, J., Kohno, K., & Sawada-Satoh, S. 2008, *ArXiv e-prints*, 805
- Hummel, E., van der Hulst, J. M., & Keel, W. C. 1987, *A&A*, 172, 32
- Jiménez-Bailón, E., Santos-Lleó, M., Dahlem, M., Ehle, M., Mas-Hesse, J. M., Guainazzi, M., Heckman, T. M., & Weaver, K. A. 2005, *A&A*, 442, 861
- Junkes, N., Zinnecker, H., Hensler, G., Dahlem, M., & Pietsch, W. 1995, *A&A*, 294, 8
- Kennicutt, Jr., R. C., et al. 2003, *PASP*, 115, 928
- Kinman, T. D. 1978, *AJ*, 83, 764
- Komossa, S., & Schulz, H. 1998, *A&A*, 339, 345
- Kotilainen, J. K., Reunanen, J., Laine, S., & Ryder, S. D. 2000, *A&A*, 353, 834
- Lawrence, A., et al. 1999, *MNRAS*, 308, 897
- Lorre, J. J. 1978, *ApJ*, 222, L99
- Maiolino, R., et al. 2003, *MNRAS*, 344, L59
- Maoz, D., Barth, A. J., Ho, L. C., Sternberg, A., & Filippenko, A. V. 2000, in *Bulletin of the American Astronomical Society*, Vol. 32, *Bulletin of the American Astronomical Society*, 1529
- Mason, R. E., Levenson, N. A., Packham, C., Elitzur, M., Radomski, J., Petric, A. O., & Wright, G. S. 2007, *ApJ*, 659, 241
- Mathis, J. S., Mezger, P. G., & Panagia, N. 1983, *A&A*, 128, 212
- Neininger, N., Guelin, M., Garcia-Burillo, S., Zylka, R., & Wielebinski, R. 1996, *A&A*, 310, 725
- Netterfield, C. B., et al. 2009, *ApJ*, submitted
- Pascale, E., et al. 2008, *ApJ*, 681, 400
- Patañchon, G., et al. 2008, *ApJ*, 681, 708
- Pérez, I., & Freeman, K. 2006, *A&A*, 454, 165
- Prunet, S., Netterfield, C. B., Hivon, E., & Crill, B. P. 2000, in *Energy Densities in the Universe, Proceedings of the XXXVth Rencontre de Moroid*
- Puget, J.-L., Abergel, A., Bernard, J.-P., Boulanger, F., Burton, W. B., Desert, F.-X., & Hartmann, D. 1996, *A&A*, 308, L5+
- Quillen, A. C., Frogel, J. A., Kuchinski, L. E., & Terndrup, D. M. 1995, *AJ*, 110, 156
- Rice, W., Merrill, K. M., Gatley, I., & Gillett, F. C. 1996, *AJ*, 112, 114
- Rieke, G. H., et al. 2004, *ApJS*, 154, 25
- Soifer, B. T., & Neugebauer, G. 1991, *AJ*, 101, 354
- Spinoglio, L., Andreani, P., & Malkan, M. A. 2002, *ApJ*, 572, 105
- Stevens, J. A., Amure, M., & Gear, W. K. 2005, *MNRAS*, 357, 361
- Stickel, M., Lemke, D., Klaas, U., Krause, O., & Egner, S. 2004, *A&A*, 422, 39
- Truch, M. D. P., et al. 2009, *ApJ*, submitted
- . 2008, *ApJ*, 681, 415
- van der Kruit, P. C., & Searle, L. 1981, *A&A*, 95, 105
- Véron, P., Lindblad, P. O., Zuiderwijk, E. J., Veron, M. P., & Adam, G. 1980, *A&A*, 87, 245
- Weingartner, J. C., & Draine, B. T. 2001, *ApJ*, 548, 296
- Wiebe, D. V. 2008, PhD thesis, University of Toronto
- Wilson, C. D., et al. 2009, *ApJ*, 693, 1736
- Wolstencroft, R. D., & Zealey, W. J. 1975, *MNRAS*, 173, 51P

TABLE 1
PHYSICAL PARAMETERS OF BLAST NEARBY GALAXIES

Galaxy	R.A. (J2000)	Dec. (J2000)	Dist. [Mpc]	Type ^(a)	Nucleus
NGC 1097	2 ^h 46 ^m 19 ^s 0	−30°16′30″	16.9 ^(b)	SB(s)b	Sy1
NGC 1291	3 ^h 17 ^m 18 ^s 6	−41°06′29″	9.7 ^(b)	(R)SB(s)0/a	...
NGC 1365	3 ^h 33 ^m 36 ^s 4	−36°08′25″	18.4 ^(c)	SB(s)b	Sy2
NGC 1512	4 ^h 03 ^m 54 ^s 3	−43°20′56″	10.4 ^(b)	SB(r)a	...
NGC 1566	4 ^h 20 ^m 00 ^s 4	−54°56′16″	18.0 ^(b)	SAB(s)bc	Sy1
NGC 1808	5 ^h 07 ^m 42 ^s 3	−37°30′47″	10.9 ^(d)	(R)SAB(s)a	Sy2
NGC 4565	12 ^h 36 ^m 20 ^s 8	+25°59′16″	12.6 ^(e)	SA(s)b	Sy2

^a RC3 morphological type from de Vaucouleurs et al. (1991)

^b Kennicutt et al. (2003)

^c Komossa & Schulz (1998)

^d Jiménez-Bailón et al. (2005)

^e Lawrence et al. (1999)

TABLE 2
OBSERVED FLUXES AND DERIVED QUANTITIES FOR BLAST NEARBY GALAXIES

Galaxy	250 μ m [Jy]	350 μ m [Jy]	500 μ m [Jy]	T_d [K]	$\log \left(\frac{M_d}{M_\odot} \right)$
NGC 1097	89.4±0.2± 7.7	40.5±0.1±3.0	16.2±0.1±1.4	21.3±0.3	... (a)
NGC 1291	26.1±0.2± 2.6	12.7±0.1±1.0	6.4±0.1±0.5	16.6±0.4	... (a)
NGC 1365	145.8±0.3±12.9	62.3±0.2±4.6	24.7±0.1±2.1	19.9±0.4	8.72 ^{+0.08} _{−0.10}
NGC 1512	14.7±0.1± 1.3	6.9±0.1±0.5	3.4±0.1±0.3	20.3±0.3	... (a)
NGC 1566	51.5±0.2± 4.6	22.2±0.1±1.7	9.1±0.1±0.8	20.1±0.4	... (a)
NGC 1808	84.0±0.1± 7.1	33.1±0.1±2.5	11.8±0.1±1.0	22.8±0.5	7.85 ^{+0.09} _{−0.11}
NGC 4565	37.2±0.5± 4.5	21.0±0.3±2.1	9.8±0.3±0.8	16.1 ^{+0.4} _{−0.5}	8.21 ^{+0.09} _{−0.11}

NOTE. — Flux uncertainties reported are first the measurement error (σ_d), and then the calibration error (σ_c). Temperatures and dust masses are extracted from the modified blackbody fits presented in Figures 8 and 9.

^a This modified blackbody fit is used to calculate κ from the DL07 model fit, so no independent mass is determined.

TABLE 3
DL07 MODEL PARAMETERS FOR BLAST NEARBY GALAXIES

Galaxy	$\log \left(\frac{M_d}{M_\odot} \right)$	$\log \left(\frac{L_d}{L_\odot} \right)$	q_{PAH} %	$\langle U \rangle$	U_{min}	γ %	χ_r^2	$\kappa^{(a)}$ m ² kg ^{−1}
NGC 1097	8.37	10.80	3.0	2.00	1.5	2.80	0.58	0.299
NGC 1291	7.62	9.42	1.6	0.46	0.4	1.10	3.47	0.290
NGC 1291 ^(b)	7.43	9.45	3.1	0.77	0.7	0.70	5.66	...
NGC 1512	7.25	9.42	3.2	1.10	1.0	0.80	0.87	0.247
NGC 1566	8.21	10.58	4.6	1.74	1.5	1.30	1.13	0.305

^a at 250 μ m

^b with constraint $U_{\text{min}} \geq 0.7$

TABLE 4
CORE FLUX FRACTIONS FOR BLAST NEARBY GALAXIES

Galaxy	Core Radius		Band	Core Flux [Jy]	Core Flux Fraction [%]
	[']	[kpc]			
NGC 1097	0.37	1.8	250	13.35±0.03	14.93±0.06
			350	4.97±0.02	12.26±0.07
			500	1.36±0.01	8.44±0.08
NGC 1291	0.71	2.0	250	1.41±0.02	5.42±0.10
			350	0.64±0.01	5.04±0.17
			500	0.23±0.01	3.58±0.17
NGC 1365	0.29	1.6	250	13.97±0.16	9.58±0.13
			350	5.38±0.10	8.62±0.19
			500	1.35±0.05	5.46±0.23
NGC 1512	0.40	1.2	250	1.51±0.01	10.26±0.08
			350	0.61±0.01	8.79±0.21
			500	0.14±0.01	3.43±0.06
NGC 1566	0.98	5.1	250	19.07±0.04	37.04±0.19
			350	7.72±0.04	34.78±0.37
			500	2.84±0.02	31.04±0.46
NGC 1808	0.29	0.9	250	10.86±0.01	12.94±0.03
			350	3.66±0.01	11.06±0.07
			500	0.92±0.01	7.79±0.05

NOTE. — Flux uncertainties reported are measurement errors (σ_d) only.